Journal of Wind Engineering & Industrial Aerodynamics 179 (2018) 200–214

Contents lists available at ScienceDirect

Journal of Wind Engineering & Industrial Aerodynamics

journal homepage: www.elsevier.com/locate/jweia

On the onset of vortex shedding past a two-dimensional porous square cylinder

K. Anirudh, S. Dhinakaran *

The Centre for Fluid Dynamics, Discipline of Mechanical Engineering, Indian Institute of Technology Indore, Simrol, Indore, 453 552, India

ARTICLE INFO

Keywords:
Darcy-Brinkman-Forccheimer model
Onset of vortex shedding
OpenFOAM
Porous square cylinder

ABSTRACT

Vortex shedding is an interesting phenomenon and a fundamental problem when it comes to flow across bluff bodies. Generation of vortices behind a porous bluff body is further compelling to study. In this paper, a numerical investigation on the onset of vortex shedding behind a porous square cylinder is presented for $41 \leq Re \leq 50$ and the computations are performed for different values of permeability (Darcy number, $Da = 10^{-6} - 10^{-2}$) and porosity ($\varepsilon = 0.629 - 0.993$). Besides, an outlook on unsteady flow across the permeable cylinder is provided for $Re = 50 - 150$. The numerical simulations are performed by modifying pimpleFoam solver of OpenFOAM 4.1 coupled with Darcy-Brinkman-Forchheimer model, using a single domain approach. Current study provides an insight on the influence of permeability on the initiation of vortex shedding behind the porous bluff body. A brief discussion is provided on the jump in flow characteristics, at intermediate values of Darcy number, comparing square with other bluff shapes. Also, a correlation for the frequency of vortex shedding is given in terms of the flow and material parameters. Optimistically, scholars and engineers working on flow control using porous media will benefit from the information presented in this article.

1. Introduction

Flow around porous bluff bodies is seen to buck the trend, owing to its relevance in several technical problems. These studies also provide engineers with a general guideline on how to apply the porous media theory for computational simplification and economy. One can directly simulate a real-time porous media case by simplifying it to a resembling porous bluff body or indirectly, by considering the overall arrangement of individual elements of the system as a single porous object. As an illustration, an outstanding numerical investigation by (Bhattacharyya et al., 2006) on porous circular cylinder can be looked into. The underlying modelling theory advocated by this article was further utilised for diverse applications like marine biological modelling (Khalili et al., 2010), modelling of circulating tumor cell detection (Swaminathan et al., 2013), aerosol respirator design (Zaripov et al., 2016), etc. Another such application of porous media is flow control (Cheung and Melbourne, 1988; Lee and Kim, 1998; Bruneau and Mortazavi, 2008; Bhattacharyya and Singh, 2011; Hasan et al., 2012; Belloli et al., 2014; Liu and Azarpeyvand, 2016; Mimeau et al., 2017) and it has also been attracting researchers recently, due to its affluent flow physics. When the fluid flows across a porous bluff body, at lower values of permeability (Darcy number, Da) and porosity (ε), the permeable body resembles its solid counterpart. However, at higher Da and ε, as more fluid enters the cylinder, distinct variations in flow trends are apparent. This occurrence is used to control the flow i.e. to suppress flow instabilities, where it is a prime concern in slender structures such as chimneys, towers and bridge decks. Amongst various porous bluff cross-sections, square cylinder is the most studied and practically relevant, and is therefore, considered in this study.

A closer rumination of the flow across porous square cylinder can be found in the literature. As stated above, at low values of Da ($\leq 10^{-6}$), almost no fluid enters through the cylinder, which makes it solid-like. But at higher Da ($\geq 10^{-6}$), fluid penetrates through, resulting in an overall reduction in drag coefficient and wake length, for lower Reynolds number (below 40) (Dhinakaran and Ponmozhi, 2011). Two recirculating wakes develop downstream the porous square cylinder in this steady flow regime. Unlike solid cylinder, at higher permeability levels, the wakes are detached from cylinder surface and they exhibit only one separation point along the horizontal axis (Yu et al., 2010). In the unsteady flow regime, at higher Re (above 40) and $Da = 10^{-6}$ (solid cylinder), drag coefficient continues to decrease, however, wake length and the frequency and intensity of vortex shedding increase (Sohankar et al.,

* Corresponding author.
E-mail address: ssdhinakar@gmail.com (S. Dhinakaran).

https://doi.org/10.1016/j.jweia.2018.03.004
Received 30 August 2017; Received in revised form 6 February 2018; Accepted 4 March 2018

Nomenclature

$\overline{C_p}$	coefficient of pressure, $(p-p_\infty)/(0.5\rho U_\infty^2)$
$\bar{s}$	velocity of fluid in porous region, (ms^{-1})
C_D	coefficient of drag, $D/(0.5\rho U_\infty^2 W)$
C_L	coefficient of lift, $L/(0.5\rho U_\infty^2 W)$
D	drag force acting on the porous cylinder (N)
d_p	diameter of the spherical particle of packed bed (m)
Da	Darcy number, κ/W^2
F	inertial factor, $(1.75/\sqrt{150})\cdot(1/\varepsilon^{1.5})$
L	lift force acting on the porous cylinder (N)
L_D	non-dimensional distance between rear face of the cylinder and the outflow boundary
P	dimensionless pressure, $p/\left(\rho_f U_\infty^2\right)$
p	pressure of the fluid, (Nm^{-2})
Pr	Prandtl number, ν/α
Re	Reynolds number, $U_\infty W/\nu$
t	dimensional time (s)
U, V	non - dimensional x, y - component of velocity, u/U_∞, v/U_∞
u, v	x, y - component of velocity (ms^{-1})
W	height of the porous cylinder
X, Y	non-dimensional horizontal, vertical distance, x/W, y/W
x, y	horizontal, vertical distance (m)

Greek

Δ	non-dimensional largest grid size
δ	non-dimensional smallest grid size
ε	porosity
κ	permeability of a material (m^2)
μ	dynamic viscosity $(kgm^{-1}s^{-1})$
ρ	density (kgm^{-3})
τ	non-dimensional time, tU_∞/W

Subscript

0	inlet value
∞	far field value
e	effective value
h	high
l	low
m	intermediate
p	particle
rms	root mean square value

1999). At $Da = 10^{-5}$ (near solid cylinder case), the vortex shedding occurs early and lasts longer in terms of Re. With better permeability (higher Da), both the period and intensity of vortex shedding decrease, followed by complete suppression beyond $Da = 10^{-2}$ (Jue, 2004). Moreover, with a larger Da, Re has to be higher before the vortices are shed alternatively (Chen et al., 2008). Porosity variation, for a constant particle diameter, does not affect results much for the same permeability level. On the contrary, for variable particle diameter, results are seen to vary significantly at different values of porosity and Darcy number. It should be noted that this variation succumbs at higher Re (Chen et al., 2009). But, the exact details on the onset of vortex shedding ($Re = 40-50$) and unsteady flow ($Re = 50-150$) around and through a porous square cylinder is nowhere to be found in the open literature.

A jump in drag coefficient at intermediate values of Darcy number (around 10^{-3}) and at $Re > 20$ is already documented for porous circular cylinder (Noymer et al., 1998) (both steady and unsteady regime) and square cylinder (Dhinakaran and Ponmozhi, 2011) (only steady regime). While this jump may exist for bodies with non-streamlined fore-bodies and short aft-bodies, more streamlined porous bodies like trapezoidal (Chen et al., 2009) and diamond cylinders (Rashidi et al., 2014) did not unveil this jump. Description of other flow tendencies at this spike regime is lacking in both steady and particular unsteady regime for porous square cylinder.

Literature on the instigation of vortex shedding in the flow behind solid bluff bodies is in abundance, since the first study on the topic (Jackson, 1987). Henderson, 1995 provide their high resolution computer simulation results for a circular cylinder near the beginning of vortex shedding. They detail the drag curve with proper quantification of viscous drag, pressure drag and base pressure coefficients. The critical Reynolds number (Re_{cr}) for the onset of vortex shedding is reported to be 46 ± 1. Both, the pressure and drag coefficients ($\overline{C_D}$) are seen to decrease up to a certain Re_{cr} value, and then increase with Re uniformly. The rise in drag coefficient value beyond Re_{cr} is credited to jump in pressure drag force (Senthil Kumar and Biswas, 2008). detailed the results of finite-element simulations used to find constants of the Landau equations for flow across a solid circular cylinder. The vortex shedding exists beyond $Re_{cr} = 45.376$ in their analysis at a critical value of Strouhal number, $St = 0.1323$. Sensitive dependency of blockage ratio on the beginning of vortex shedding is also pointed out in their analysis. Sohankar et al., 1995 carried out numerical calculations of vortex shedding past a square cylinder, at $Re = 45$–200 for 5% blockage ratio. Their results suggest that onset of vortex shedding occur between $Re = 50$–55 and beyond this, the flow develops to exhibit well-defined vortex shedding frequency. In a more recent numerical work (Sohankar et al., 1998), arrived at a more accurate value of $Re_{cr} = 51.2 \pm 1$ for the same numerical setup. In an experimental attempt (Sohankar et al., 1997), however, they declared $Re_{cr} = 47 \pm 2$ for practically zero-blockage ratio configuration. It is clear that critical Reynolds number for commencement of vortex shedding increases with blockage ratio. Also, at $\alpha = 45^\circ$ (diamond cylinder), onset occurs at $Re_{cr} = 42 \pm 1$, showing that vortices shed early as inclination angle increases. Sohankar et al., 1999 simulated unsteady, incompressible 2D flow around a solid square cylinder at incidence, at $Re = 45-200$. Influence of blockage ratio and inclination angle on the overall flow behaviour, particularly origination of vortex shedding is stated. They have observed that the flow behaviour at low angles of incidence (particularly at $\alpha \leq 20^\circ$) is distinct from the fully separated flow at higher angles of incidence. At zero angle of incidence, they have reported Re_{cr} to be 51.2 ± 1. Sharma and Eswaran, 2004 presented numerical results which agree with the earlier onset regime (Sohankar et al., 1997, 1999). The mean recirculation length (L_R) and $\overline{C_D}$ are stated to decrease, while St and root mean square value of lift coefficient ($(C_L)_{rms}$), are observed to increase as Re is increased due to higher momentum. Lankadasu and Vengadesan, 2008 studied the influence of a linear shear at inlet on the onset of vortex shedding, and its corresponding effect on mean drag coefficient. A critical Reynolds number of $Re_{cr} = 46 \pm 1$, 43 ± 1 and 39 ± 1 is recorded for shear parameter values of 0, 0.1 and 0.2, respectively. They have noticed that the instigation of vortex shedding is pre-poned and mean drag coefficient decreases as the shear parameter is increased. Knowledge of vortex shedding commencement is also made available for other bluff body shapes recently. Paul et al., 2014 proclaimed $Re_{cr} = 512.5 \pm 0.5$, 231.5 ± 0.5, 87.5 ± 0.5 and 64.5 ± 0.5 for different axis ratio values (ratio of major to minor axes) of 0.1, 0.4, 0.6 and 0.8, respectively for unconfined flow domain. A critical Reynolds number between 69 and 70 was predicted for the flow across a solid semi-circular cylinder by Kumar et al., 2016 for a confined domain (25% blockage ratio). In summary, the flow characteristics differ before and after the onset of vortex shedding significantly, and the same is very sensitive to shear parameter, blockage ratio, axis ratios and inclination of the incoming flow.

From the above discussion, it is clear that the onset of vortex shedding and unsteady flow around a solid bluff body is both quantitatively and qualitatively well-discerned. But the exact details of the same for a porous bluff body, particularly porous square cylinder is missing. In the present numerical attempt, the discussion on flow across porous square cylinder is extended from steady regime to the onset of vortex shedding and a brief outlook on unsteady flow regime is provided. The present manuscript details on the above mentioned spike in the flow parameters at intermediate Darcy number values and a detailed perspective on flow traits like drag ratio, wake length, critical Reynolds number, root mean square values of coefficient of lift and Strouhal number is presented. Variation in the occurrence of vortex shedding across porous bluff bodies in the intermediate Darcy regime ($Da = 10^{-4} - 10^{-3}$) is also highlighted.

2. Mathematical formulation

2.1. Problem description

A pictorial representation of the problem under consideration is displayed in Fig. 1. A fixed porous square cylinder of size 'W', subjected to a cross flow with uniform free stream velocity (U_∞), is placed in an unconfined domain. Artificial boundaries are placed sufficiently far away from the cylinder with an intention to make the problem computationally feasible. It is well-understood that during initiation of vortex shedding, the flow is always two-dimensional, and accordingly, the computational setup is retained two-dimensional (Schumm et al., 1994). In order to make the problem amenable to numerical simulations, it is assumed that the flow is laminar and incompressible and the effective viscosity of the porous medium and fluid is equal. The porous cylinder is taken to be isotropic, homogeneous and remains saturated throughout with a single-phase fluid. Single set of equations are used to describe the flow in both, fluid and porous region, popularly known as the Single Domain Approach (Bhattacharyya et al., 2006).

2.2. Governing equations

With the above mentioned assumptions, the flow in clear fluid region is modelled by Navier-Stokes equation, given as,

Continuity Equation:

$$\frac{\partial u}{\partial x} + \frac{\partial v}{\partial y} = 0. \tag{1}$$

Momentum Equations:

$$\rho\left(\frac{\partial u}{\partial t} + u\frac{\partial u}{\partial x} + v\frac{\partial u}{\partial y}\right) = -\frac{\partial p}{\partial x} + \mu_e\left(\frac{\partial^2 u}{\partial x^2} + \frac{\partial^2 u}{\partial y^2}\right), \quad \text{and,} \tag{2}$$

$$\rho\left(\frac{\partial v}{\partial t} + u\frac{\partial v}{\partial x} + v\frac{\partial v}{\partial y}\right) = -\frac{\partial p}{\partial y} + \mu_e\left(\frac{\partial^2 v}{\partial x^2} + \frac{\partial^2 v}{\partial y^2}\right). \tag{3}$$

A few modifications in the above governing equations need to be performed for modelling the flow in porous region. It is well-known that superficial velocity of the flow through porous media means the artificial flow velocity by which flow would occur in the absence of porous material i.e., when the presence of porous medium is disregarded. Superficial velocity is relied on because it is readily known and is unambiguous, while the physical or actual velocity may vary with location inside the complex porous region and it is hard to determine. It is obvious that the existence of porous medium will reduce the area available for the superficial flow oozing through the pores, inturn increasing the velocity higher than the rest of the domain. The proper entity that can relate the physical velocity in the porous region and the superficial velocity outside is called porosity, which is nothing but the volume fraction of the voids present in the medium. Hence, the physical velocity is related to the superficial velocity as $\bar{s} = v/\varepsilon$ and this introduces the '$1/\varepsilon$' term next to velocity terms in the transport equation (Holdich, 2002). Further, two source terms are introduced in the momentum equation for modelling the flow in porous region. The first source term is Darcy term, which takes into account the existence of general porous resistance in the flow. Brinkman coefficient (advection term along with porosity) brings into the viscous resistance offered by porous zone to the fluid flow. At higher Re, Forchheimer term, the second source term, looks after the inertial resistance offered by the porous media. This Darcy-Brinkman-Forchheimer extended model is the most applied numerical approach when it comes to flow through porous media (Dhinakaran and Ponmozhi, 2011). The governing equations (Wu and Wang, 2010) solved in the present numerical computations in porous region are given as,

Continuity Equation:

$$\frac{\partial u}{\partial x} + \frac{\partial v}{\partial y} = 0. \tag{4}$$

Momentum Equations:

$$\rho\left(\frac{1}{\varepsilon}\frac{\partial u}{\partial t} + \frac{u}{\varepsilon^2}\frac{\partial u}{\partial x} + \frac{v}{\varepsilon^2}\frac{\partial u}{\partial y}\right) = -\frac{\partial p}{\partial x} + \frac{\mu_e}{\varepsilon}\left(\frac{\partial^2 u}{\partial x^2} + \frac{\partial^2 u}{\partial y^2}\right) - \frac{\mu}{\kappa}u - \frac{\rho F}{\sqrt{\kappa}}\left|\vec{V}\right|u, \quad \text{and,} \tag{5}$$

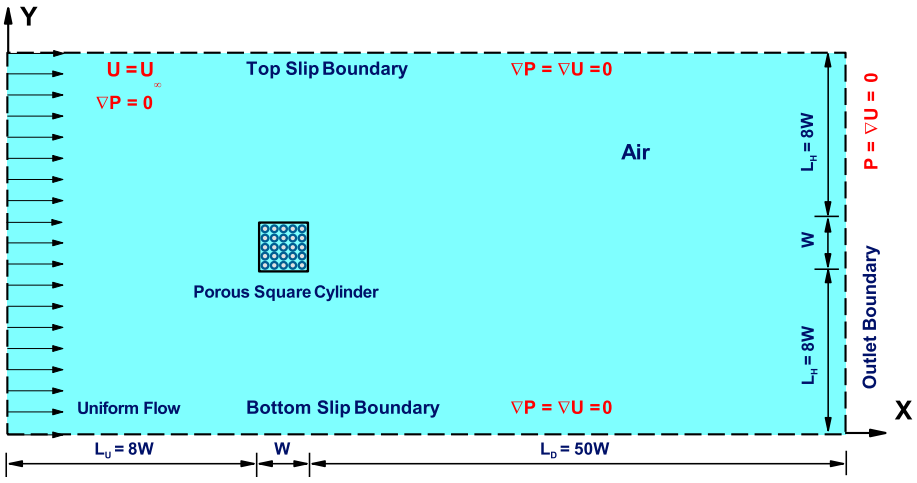

Fig. 1. Schematic diagram of the computational set-up (along with the boundary conditions) for the unconfined flow around and through a permeable square cylinder.

$$\rho\left(\frac{1}{\varepsilon}\frac{\partial v}{\partial t}+\frac{u}{\varepsilon^2}\frac{\partial v}{\partial x}+\frac{v}{\varepsilon^2}\frac{\partial v}{\partial y}\right)=-\frac{\partial p}{\partial y}+\frac{\mu_e}{\varepsilon}\left(\frac{\partial^2 v}{\partial x^2}+\frac{\partial^2 v}{\partial y^2}\right)-\frac{\mu}{\kappa}v-\frac{\rho F}{\sqrt{\kappa}}\left|\vec{V}\right|v. \quad (6)$$

In the above equations, $\left|\vec{V}\right| = \sqrt{u^2+v^2}$ is the resultant velocity and $F = \frac{1.75}{\sqrt{150}}\cdot\frac{1}{\varepsilon^{1.5}}$ is the inertial factor (Dhinakaran and Ponmozhi, 2011).

2.3. Non-dimensionalisation of results

Since, using non-dimensional variables in OpenFOAM 4.1 is quite cumbersome, non-dimensionalisation of the output variables is done post-simulation, by using the characteristic scales

$$X=\frac{x}{W},\ Y=\frac{y}{W},\ \tau=\frac{tU_\infty}{W},\ P=\frac{p}{\rho U_\infty^2},\ U=\frac{u}{U_\infty}\ \text{and}\ V=\frac{v}{U_\infty}. \quad (7)$$

2.4. Boundary conditions

As shown in Fig. 1, a uniform horizontal flow is fed at the inlet of the domain i.e. $U=1$ and $V=0$. At outlet of the domain, a zero-Gradient boundary condition is imposed for velocity field and absolute pressure is kept to be zero i.e., $P=0$ and $\nabla U=0$. At the top and bottom boundary of the numerical domain, slip boundary condition for velocity is applied and the pressure gradient is kept to be zero throughout.

2.5. Relating porosity and permeability

Porous cylinder in the current simulations is assumed to be made up of a packed bed of spherical particles. The number of these particles, their size, void between them and their connectivity decide how porous and permeable the medium is to the flow through it. Usually, during flow through porous media, porosity and permeability are varied independently. While these parameters change, particle diameter (d_p) and/or number of particles in the medium vary, which changes the topography of entire medium during the simulation process. Hence, for the sake of uniformity, non-dimensional size of the spherical particles comprising the medium is kept uniform throughout all computations to '$d_p/W = 0.01$'. The porosity and permeability terms are linked together through the Carman-Kozeny relation (Dhinakaran and Ponmozhi, 2011), which is given by

$$Da=\frac{1}{180}\frac{\varepsilon^3}{(1-\varepsilon)^2}\left(\frac{d_p}{W}\right)^2=5.56\times10^{-7}\cdot\frac{\varepsilon^3}{(1-\varepsilon)^2}. \quad (8)$$

3. Numerical details

Numerical computations performed for meeting the present cause are based on finite volume method and the opensource tool OpenFOAM 4.1 (Weller et al., 1998) is used. The generic pimpleFOAM solver (based on the combination of SIMPLE and PISO algorithm) of OpenFOAM 4.1 is modified by applying the Darcy-Forchheimer-Brinkman model. This solver helps to adjust the Courant number to a higher value, inturn speeding up the simulations to achieve a stable solution due to under-relaxation. Gauss linear scheme is used to account for time derivative, gradient, divergence and Laplacian terms and QUICK interpolation scheme are used for the collocated grid. Further, the PCG solver with DIC pre-conditioner and the smoothsolver with symGaussSiedel smoother are used for evaluating the pressure and velocity terms. The residual criteria for both the terms is set to be 10^{-10}, no under-relaxation is applied and the nOuterCorrectors are set to 50, nCorrectors to 2 and NonOrthogonalCorrectors to 0. Although OpenFOAM 4.1 does not use an explicit Rhie-Chow correction, the generic correction for pressure terms is believed to be Rhie-Chow inspired. The average values of velocity field is evaluated for one complete cycle of lift coefficient (C_L). The time-averaged streamline and vorticity contours are evaluated from averaged velocity field. Also, the drag force and pressure values are averaged for the same, one complete cycle of C_L. It should be noted that the lift coefficient cycle is selected once after the C_L reaches unsteady periodic nature.

4. Grid generation and code validation

The generic blockMesh tool is employed for the generation of a structured non-uniform mesh in the computational domain. Intricate flow phenomena occurring in the porous region and at the fluid-porous interface needs special attention. Owing to this fact, a fine uniform mesh is used in the porous cylinder and a region of $0.5W$ around it, with an element size of $\delta = 0.01W$ (Sharma and Eswaran, 2004). A non-uniform mesh with simple grading further extends up to a distance of $7.5W$ around the cylinder, with maximum element size of $\Delta = 0.2W$. A uniform mesh is extended downstream of the cylinder beyond this non-uniform mesh with $\Delta = 0.2W$ up to the downstream length (L_D). A grid sensitivity analysis is conducted at $Re = 50$ and $Da = 10^{-6}$, to check the dependence of flow parameters i.e. $(C_D)_{rms}$, $(C_L)_{rms}$ and St on the grid size and downstream length. Numerous test simulations were run learning about the optimal grid size for three different downstream lengths viz., $L_D = 40W$, $50W$ and $60W$. Since, the study deals with understanding the critical Reynolds number for onset of vortex shedding, it is made sure that the resulting value of Re_{cr} is domain independent and accordingly, a larger downstream length is chosen. Also, from the literature, it is well-understood that the blockage ratio increases the critical Reynolds number value, therefore, simulations were also run for different domain height viz., 16 W, 18 W and 20 W for $Da = 10^{-6}$ and $Re = 44$. For all the cases, Re_{cr} remained unchanged and hence, keeping computational economy in mind the domain height of $16W$ is selected. From the literature (Sohankar et al., 1998; Sharma and Eswaran, 2004; Franke et al., 1990), it is well understood that the root-mean-square values of global quantities are more sensitive to the distance of first grid point away from the cylinder. Hence, the first grid point around the porous cylinder is kept at 0.02 W, 0.015 W, 0.01 W and 0.0075 W away and the current solver is tested for four different grids of $X \times Y$ sizes viz., 377×154 (Grid A), 422×191 (Grid B), 505×262 (Grid C) and 566×317 (Grid D), respectively. Table 1 gives the details of the grid-independence study for different downstream lengths. After a close observation of the given values, keeping both accuracy and computational economy into perspective, Grid C at $L_D = 50$ is chosen. A depictive representation of the Grid C with the current numerical domain is shown in Fig. 2.

It is well-known that a porous cylinder behaves similar to its solid counterpart at low values of Darcy number, $Da = 10^{-6}$. Consequently, to verify the current solver, the computed results at this low Da value were compared with the results for the case of a solid square cylinder by Sharma and Eswaran, 2004 and porous square cylinder by Dhinakaran and Ponmozhi, 2011. Satisfactory confidence with the numerical results of these studies is obtained, and the details are given Tables 2 and 3. Also, the darcyFoam solver's feasibility for modelling porous media condition is further validated with Dhinakaran and Ponmozhi, 2011 at an intermediate value of Darcy number, $Da = 10^{-3}$. Different flow parameters viz., C_D, St and L_R displayed well agreement with the literature values, facilitating the confidence to proceed ahead with the problem in hand (see Table 4).

5. Results and discussions

The transition of flow from steady to unsteady flow regime is looked into in this study and hence, Re is varied between $41 \le Re \le 50$. Also, some discussion about the flow structures in the unsteady flow regime is provided for $50 \le Re \le 150$. Different Darcy number values of 10^{-6}, 10^{-4} and odd multiples of 10^{-3} and 10^{-2} are used to appropriately model the porous body as impermeable and permeable with varying levels of permeability. As mentioned in Sec. 2.5, Carman-Kozeny relation is used

Table 1
Grid sensitivity and downstream length dependence test on Strouhal number (St), drag coefficient (C_D) and recirculation length (L_R) at $Da = 10^{-6}$ and $Re = 50$.

L_D	$(C_D)_{rms}$			$(C_L)_{rms}$			St		
	40	50*	60	40	50*	60	40	50*	60
Grid A (377 × 154)	1.6630	1.6630	1.6631	0.0447	0.0448	0.0449	0.2333	0.2333	0.2334
Grid B (422 × 191)	1.6685	1.6685	1.6686	0.0472	0.0472	0.0473	0.2336	0.2336	0.2337
Grid C* (505 × 262)	1.6740	1.6740	1.6741	0.0496	0.0496	0.0497	0.2338	0.2338	0.2340
Grid D (566 × 317)	1.6743	1.6743	1.6744	0.0504	0.0504	0.0505	0.2339	0.2339	0.2342

Note: * indicates the mesh size and L_D used in the study.

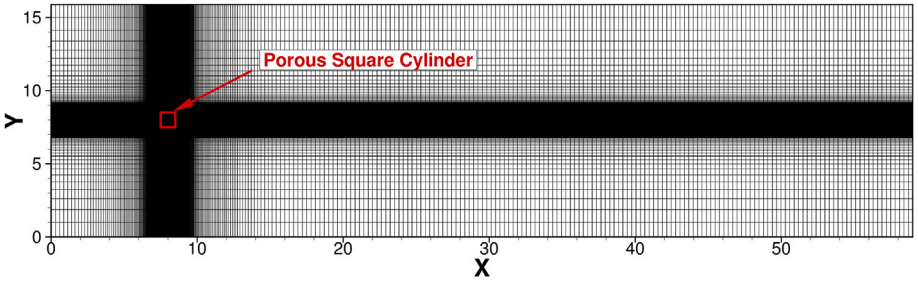

Fig. 2. Non-uniform mesh distribution in the computational domain for the present simulations.

Table 2
Comparison of drag coefficient (C_D), recirculation length (L_R) and Strouhal number (St) for different Re and $Da = 10^{-6}$.

Re	Drag Coefficient (C_D)				Recirculation length (L_R)			
	a[a]	b[b]	Present Study	% Deviation	a[a]	b[b]	Present Study	% Deviation
10	3.3750	3.3207	3.2070	2.2796	0.6450	0.6500	0.6650	2.3077
20	2.4020	2.3750	2.3550	0.8421	1.3000	1.3900	1.4000	0.7194
30	2.0140	2.0100	1.9820	1.3930	1.9850	2.1100	2.1400	1.4218
40	1.7980	1.8040	1.7660	2.1064	2.6650	2.8220	2.8810	2.0907
50	–	1.6570	1.6705	0.8147	–	2.9840	3.0115	0.9216
75	–	1.5490	1.5639	0.9619	–	2.2263	2.2051	0.9523
100	–	1.4947	1.5120	1.1574	–	1.9157	1.8896	1.3624
150	–	1.4655	1.4860	1.3970	–	1.5947	1.5719	1.4297

Column *a*: Dhinakaran and Ponmozhi (2011) and Column *b*: Sharma and Eswaran (2004).

Table 3
Comparison of drag coefficient (C_D), recirculation length (L_R) and Strouhal number (St) for different Re and $Da = 10^{-6}$.

Re	Strouhal number (St)		
	a[a]	Present Study	% Deviation
50	0.1175	0.1169	0.5106
75	0.1370	0.1374	0.2920
100	0.1485	0.1496	0.7407
150	0.1590	0.1599	0.5597

Column *a*: Sharma and Eswaran (2004).

Table 4
Comparison of drag coefficient (C_D) and recirculation length (L_R) for different values of Re at $Da = 10^{-3}$.

Re	Drag Coefficient (C_D)			Recirculation length (L_R)		
	a[a]	b[b]	c[c]	a[a]	b[b]	c[c]
1	14.6196	14.2650	2.4255	–	–	–
5	4.7786	4.7174	1.2807	0.1169	0.1151	1.5398
10	3.2616	3.2406	0.6439	0.5246	0.5323	1.4678
20	2.3652	2.3475	0.7484	1.1785	1.1930	1.2304
30	2.0255	2.0021	1.1553	1.9415	1.9820	2.0860
40	1.8468	1.8171	1.6082	2.7739	2.8623	3.1868

Column *a*: Dhinakaran and Ponmozhi (2011); Column *b*: Present Study; Column *c*: Deviation from the results presented in Column *a*.

to select the minimum required porosity value for these levels of permeability. For a better discussion of the numerical results, three different permeability zones have been identified. These zones are lower (Da_L), intermediate (Da_M) and higher Da (Da_H) zones, which represent $10^{-6} \leq Da \leq 10^{-4}$, $10^{-4} < Da \leq 4 \times 10^{-3}$ and $4 \times 10^{-3} < Da \leq 10^{-2}$, respectively.

5.1. Time evolution of lift and drag coefficients

The transition between steady and unsteady flow regimes is looked into, and hence, both steady and unsteady flow behaviour is seen for the current Reynolds number range. As discussed earlier in Sec. 1, when the Reynolds number increases above a certain critical value, vortices in the separation bubble start separating alternatively from the trailing edge of the porous cylinder and move downstream. This phenomenon is referred to as vortex shedding and this paper primarily deals with onset of the same. Time evolution trends of both C_L and C_D are shown is Fig. 3 for $Re = 50$, at various Darcy number values. For $Re < Re_{cr}$, flow remains steady after an initial transition for all permeability levels. But for $Re > Re_{cr}$, the flow transits from steady to unsteady behaviour, by exhibiting uniform oscillations in both C_L and C_D curve. Furthermore, a graphical representation of C_L curve is given in Fig. 4 for understanding the effect of permeability on vortex shedding intensity. As Darcy number increases, amount of fluid flowing through the cylinder also increases. This results in depletion of boundary layer around the cylinder and a reduction in overall pressure gradient across the porous body. The result would be

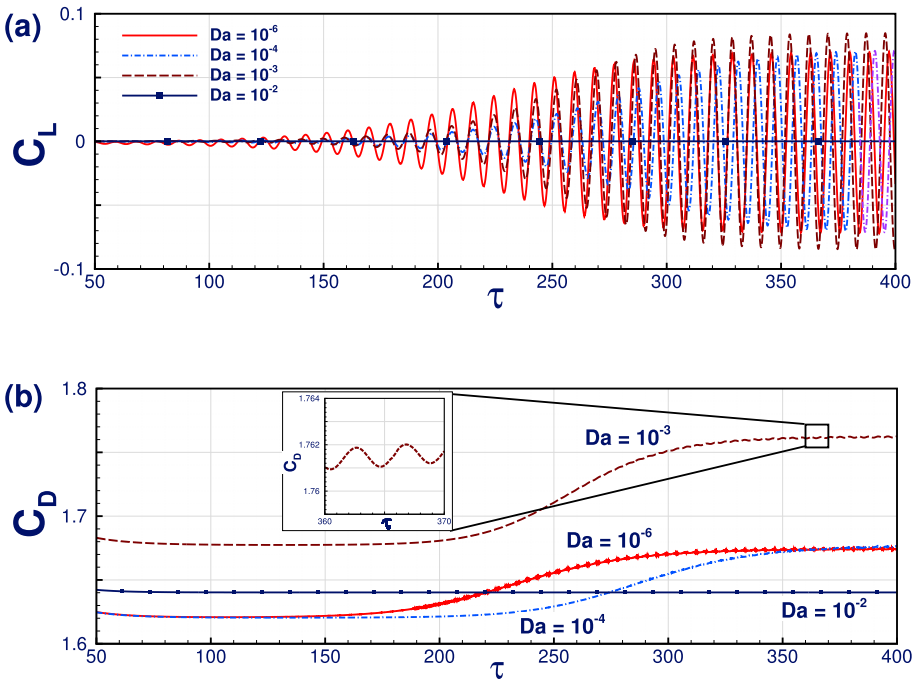

Fig. 3. Time evolution of (a) lift coefficient, C_L and (b) drag coefficient, C_D for different values of Darcy numbers ($Da = 10^{-6}$, 10^{-4}, 10^{-3} and 10^{-2}) at Reynolds number, $Re = 50$. Legend in sub-figure (a) is also applicable to sub-figure (b).

suppression of vortex shedding, as both viscous and inertial resistances to the flow decrease and the same is witnessed in Fig. 4(a) and 4(j). However, beyond Da_M zone, in contrast to the above belief, an increase in C_L amplitude is clear up to $Da = 10^{-3}$ (4(c) - 4(g)). As the permeability level is further increased, intensity of vortex shedding drastically reduces at the end of Da_M zone, as shown in Fig. 4(h) and 4(i) and it further gets completely suppressed after $Da = 5 \times 10^{-3}$ (4(j)) in the Da_H zone. A visual representation of this phenomenon is provided in the following section.

5.2. Instantaneous streamline and vorticity contours: onset of vortex shedding and unsteady flow regime

In general, the shear layer around a bluff body is comprised of boundary layer, separating free shear layer and wake forming downstream. In the steady flow regime ($Re < Re_{cr}$), the wake region comprises of a steady recirculation, with two symmetrically placed vortices on the either side of the wake, as discussed above in Sec. 5.1. At a critical Re value, this recirculation region develops unsteadiness, firstly from the downstream end of the bubble, as observed in Fig. 5. As more fluid is pumped with increasing Re, strength and amplification of this bubble increases ahead. Unsteadiness in this wake, while the flow speed outside this region becomes overwhelming, induces asymmetry and finally, the wake starts shedding vortices into the stream.

In Fig. 5 the instantaneous streamilne contours, at the topmost point of C_L curve oscillations, are plotted at, just before and just after the critical Reynolds number point. The above flow physics is well detailed in these contours. For Da_L zone, the wake is seen to be attached to the rear cylinder surface just before the onset of vortex shedding. At Re_{cr}, stability of wakes is compromised, and it breaks into alternate shedding of vortices, with weak oscillations as shown in Fig. 6 during a cycle of vortex shedding. Reduction in the intensity of vortex shedding as permeability is increased from $Da = 10^{-6}$ to $Da = 10^{-4}$ (mentioned in Sec. 5.4), is witnessed in Fig. 5(i) and (ii), at a particular Re due to increased through flow. When the permeability level is increased ahead, inspite of higher through flow, the vortices shed early at $Re_{cr} = 42$ for $Da = 10^{-3}$ in the Da_M zone. The reason is ascertained to jump phenomenon which shall be reasoned in the section to follow.

Unsteady flow structures can be seen in Figs. 7 and 8, wherein the effects of permeability variation on the flow around permeable square cylinder is brought out through time-averaged mean flow for $Re = 50$, 100 and 150. It can be visualised that position and size of the vortex are found to be varying at different Re and Da values. It should be noted that in comparison to instantaneous flow contours, the time-averaged flow patterns offer a better pictorial representation of the influence of permeability in the downstream region of the cylinder. Time-averaged flow displays a twin wake structure behind the porous cylinder. Reattachment point of these wakes is seen to move towards the cylinder surface and resultingly, wake length is found to decrease, while the wakes are found to be bulging with increasing Re. Also, as seen in Fig. 9, for a given Re, reattachment point of wakes clearly begins moving away from the cylinder as Da increases. However, the size of wake structure shrinks at higher values of permeability due to lesser resistance to the flow and increased penetration of fluid through cylinder. In Da_M zone, at $Da = 10^{-3}$, in accordance to the jump phenomenon, this occurrence does not appear and like increasing Re case, reattachment point moves towards the cylinder with increasing wake width. Such happenings clearly suggest an increase in the vortex shedding intensity from the porous cylinder. In Da_H zone, at $Da = 10^{-2}$, the wake structure seems to be completely suppressed and fluid penetrates through the cylinder with very less or no deviation at all. As permeability of the porous cylinder is increased from the solid-like condition, fluid starts penetrating through the cylinder. Deviation of this penetration is seen to succumb with rising Da due to reduction in inertial and viscous resistances in the porous zone. Variation in wake size in time-averaged streamline contours explains about the influence of permeability on vortex shedding.

In Fig. 8(a), instantaneous vorticity contours are presented, while in Fig. 8(b) the same are time-averaged over once cycle of lift coefficient at $Re = 150$ for $Da = 10^{-6}$, 10^{-4}, 10^{-3} and 10^{-2}. Fig. 8(a) depicts alternate positive and negative vortices being shed from the porous square cylinder, except for $Da = 10^{-2}$. In the Da_L zone, more amount of shear stress is exerted in comparison to the other porous zones. Resultingly, fluid particles near the porous surface start rotating, imparting their motion to the flow field downstream. In Da_M and Da_H zones, velocity

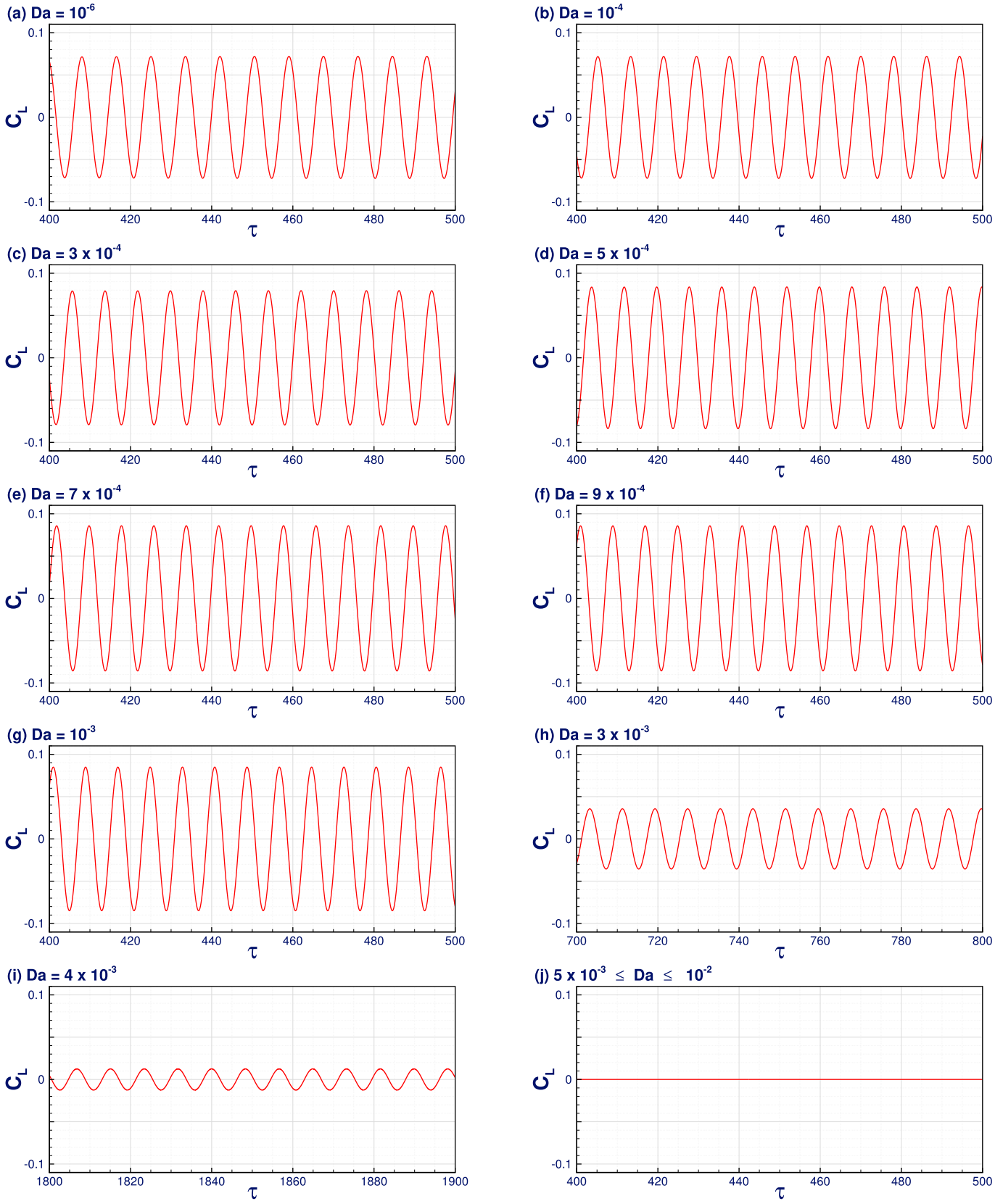

Fig. 4. Time evolution of coefficient of lift, C_L at different values of Darcy number at Reynolds number, $Re = 50$.

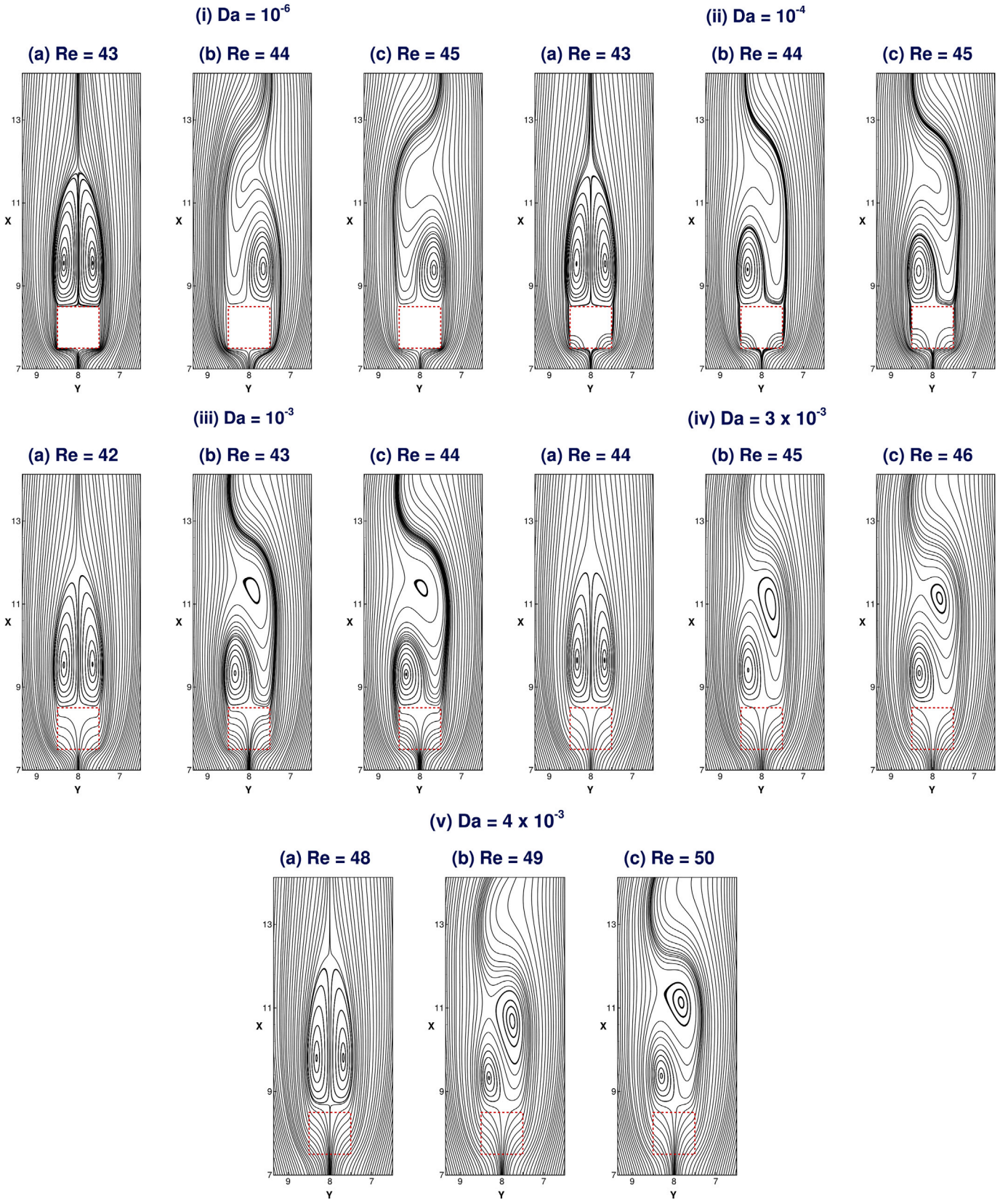

Fig. 5. Streamline contours at different values of Darcy number and Reynolds number, (a) just before, (b) at and (c) just after the critical Reynolds number for onset of vortex shedding.

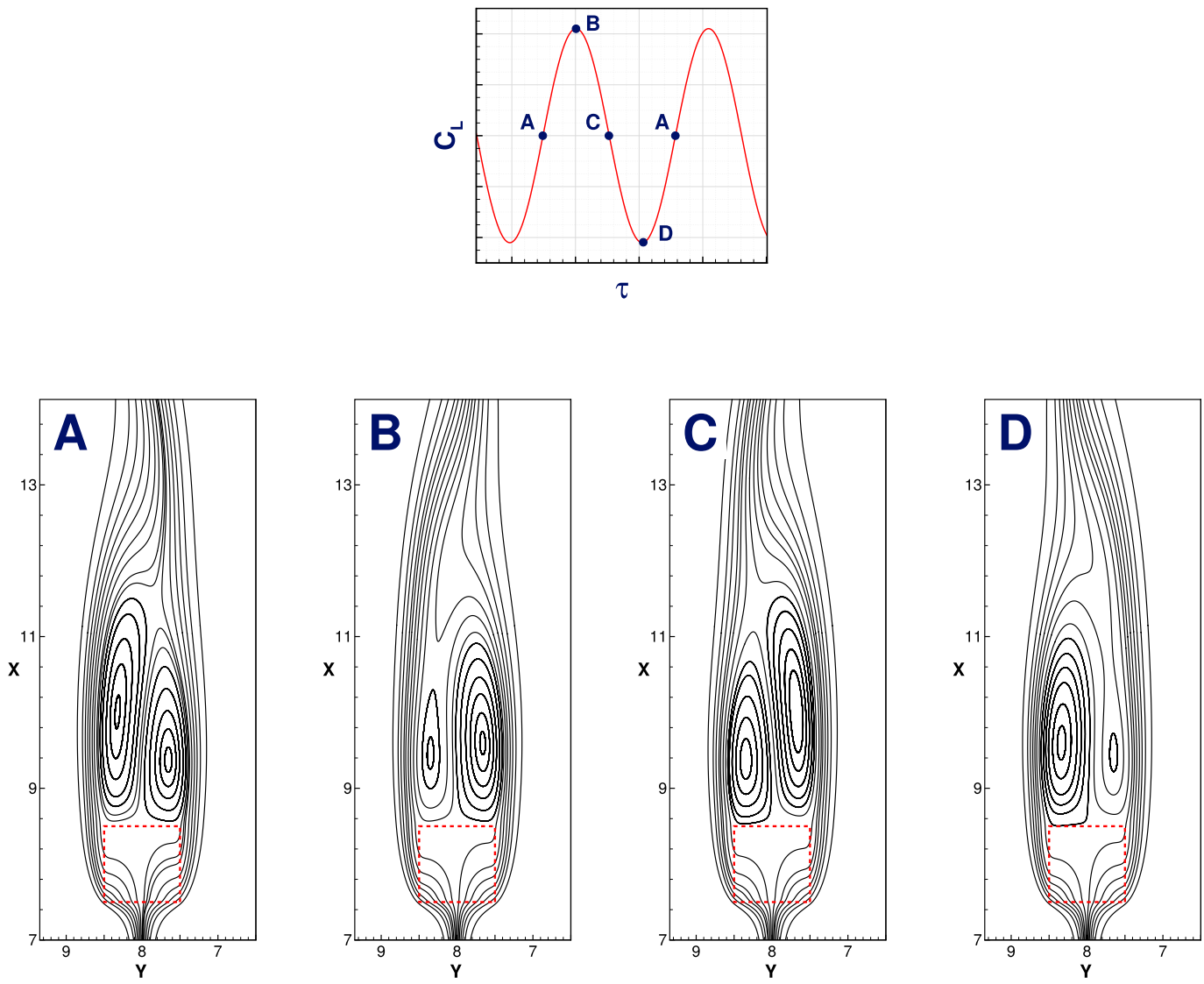

Fig. 6. Wiggling of the wake behind the porous square cylinder on the verge of vortex shedding at $Da = 10^{-3}$ and $Re = 42$ at different time instants (A, B, C and D) during one vortex shedding cycle.

gradient across the porous cylinder declines due to higher *Da* values, inturn depleting the hydrodynamic boundary layer. As seen in successive frames of Fig. 8(a), this occurrence prevails more significant for frontal surface and hence, more amount of fluid oozes through this face of the porous cylinder. For offering a better insight on the influence of permeability on the vorticity around the porous cylinder, time-averaged vorticity contours are given. It is seen that with increasing *Re*, the time-averaged vorticity contours tend to shift away from the symmetry line, hinting about the increasing intensity of vortex shedding. Similar behaviour is seen to display while increasing *Da*, in Da_M zone for $Re_{cr} \leq Re \leq 100$. Vorticity contours for $Da = 10^{-6}$ and 10^{-4} appear almost same at all values of *Re*. However, for $Re \geq 100$ at $Da = 10^{-3}$, the vorticity contours shift towards the symmetry line, as shown in Fig. 8(b)(iii). This suggests a reduction in intensity of vortex shedding, at higher values of *Re*. Further, at $Da = 10^{-2}$, the voriticty contours tend to converge towards the symmetry line, stretching away from the porous body. But this convergence appears to happen at infinity, suggesting complete suppression of vortex shedding due to through flow.

When the fluid flows across a porous body, fluid velocity along the surface is primarily governed by the permeability and Reynolds number. This velocity, unlike for a solid body, is not maintained zero throughout the surface. Hence, when compared to the solid body, velocity differs the vorticity production rate on the porous surface. Furthermore, transport of vorticity along the shear layer behind the porous body is also changed by the superficial velocity. Therefore, as the permeability of the porous body is increased, more fluid flows through the cylinder and hence, variation in flow structure is evident. Especially, in the Da_H regime, the vortex shedding is witnessed to suppress and standing recirculation region is seen. At such high values of permeability, the wake no longer stays attached to the surface as in a solid body, but detaches and moves away from the porous surface. This happens due to less resistance to the flow in comparison to impermeable condition, so that the flow loses momentum after penetrating the porous body and forms recirculation region distant downstream from the rear porous surface. Similar occurrences are seen through Fig. 9, wherein the wake both, moves away from the cylinder and shrinks in size. This region inevitably disappears between $Da = 9 \times 10^{-3}$ and $Da = 10^{-2}$ for all values of *Re*.

From the above discussion, it can be understood that the permeability of porous square cylinder has a deep influence on the hydrodynamic characteristics in and around the cylinder.

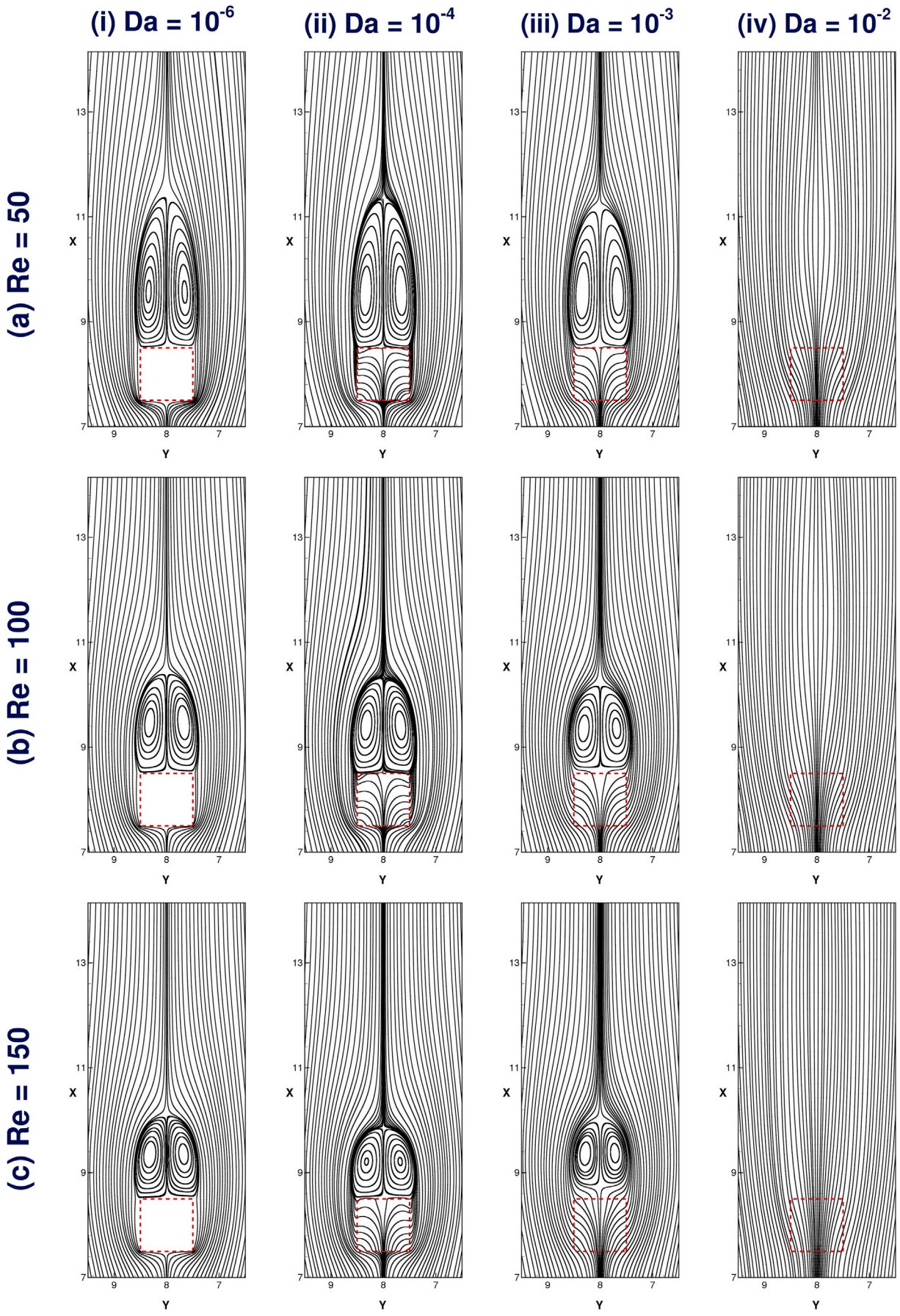

Fig. 7. Streamline contours for time-averaged flow across porous square cylinder at (a) $Re = 50$, (b) $Re = 100$ and (c) $Re = 150$ for various Da values.

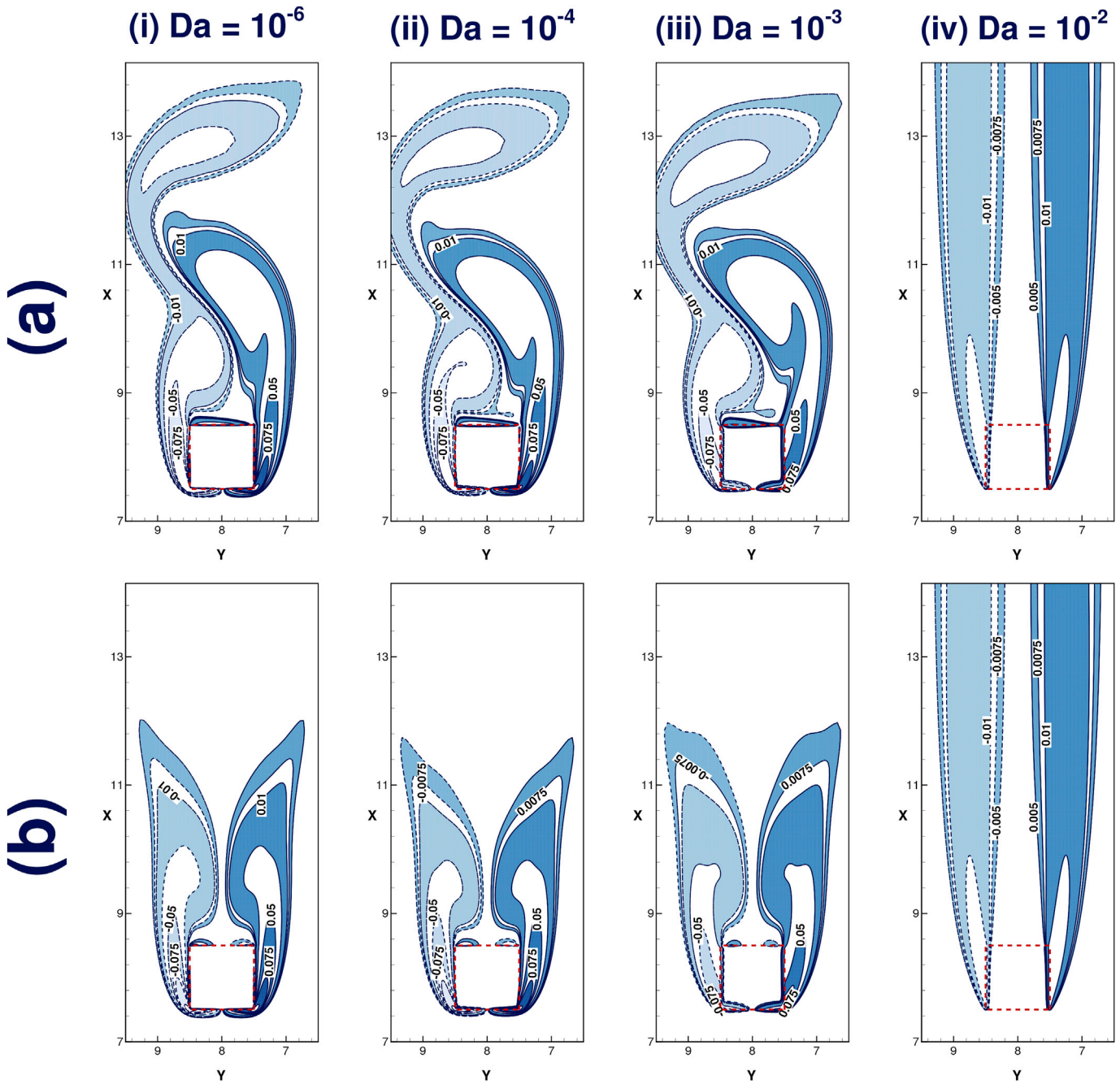

Fig. 8. (a) Instantaneous and (b) time-averaged vorticity contours for flow across porous square cylinder at $Re = 150$ for various Da values.

5.3. *Distribution of time-averaged pressure coefficient ($\overline{C_p}$)*

The 'jump' in the flow characteristics portrayed in the above discussions is attempted to be reasoned in this section. Distribution of pressure coefficient is displayed in Fig. 10 at different velocity i.e., different Re values and levels of permeability. It is well-understood that at as the Reynolds number increases, dominance of pressure drag force over that of viscous drag force increases. Hence, the variation of pressure coefficient across the porous cylinder is utilised to understand the particular intimidating jump phenomenon discussed in the preceding sections. In Fig. 10(a), for $Re = 50$, pressure gradient across the front and rear surface of the cylinder appears to be almost similar for $Da = 10^{-6}$ and 10^{-4}. Furthermore, the pressure gradient for $Da = 10^{-3}$ is seen to augment compared to Da_L zone and as the permeability is increased beyond, a steep decrease in $\overline{C_p}$ difference at front and rear face is evident for $Da = 10^{-2}$. However, in more recent studies conducted for porous diamond (Vijaybabu et al., 2018) and triangular cylinder (Vijaybabu et al., 2018b) in the steady and unsteady flow regimes, such anomalous variation in coefficient of pressure distribution, rather jump in flow characteristics has not been reported. It should be noted that such jump in flow parameters has been highlighted by Noymer et al., 1998 for porous circular cylinder in steady and unsteady flow regime and Dhinakaran and Ponmozhi, 2011 and Vijaybabu et al., 2017 in steady flow regime for the case of porous square cylinder. Other porous body cross-sections like trapezoidal (Chen et al., 2009) and diamond (Rashidi et al., 2014) cylinder does not show any kind of jump in drag ratio or other flow parameters. A closer rumination of such variation in flow parameters amongst different cross-sections of porous bodies suggest that

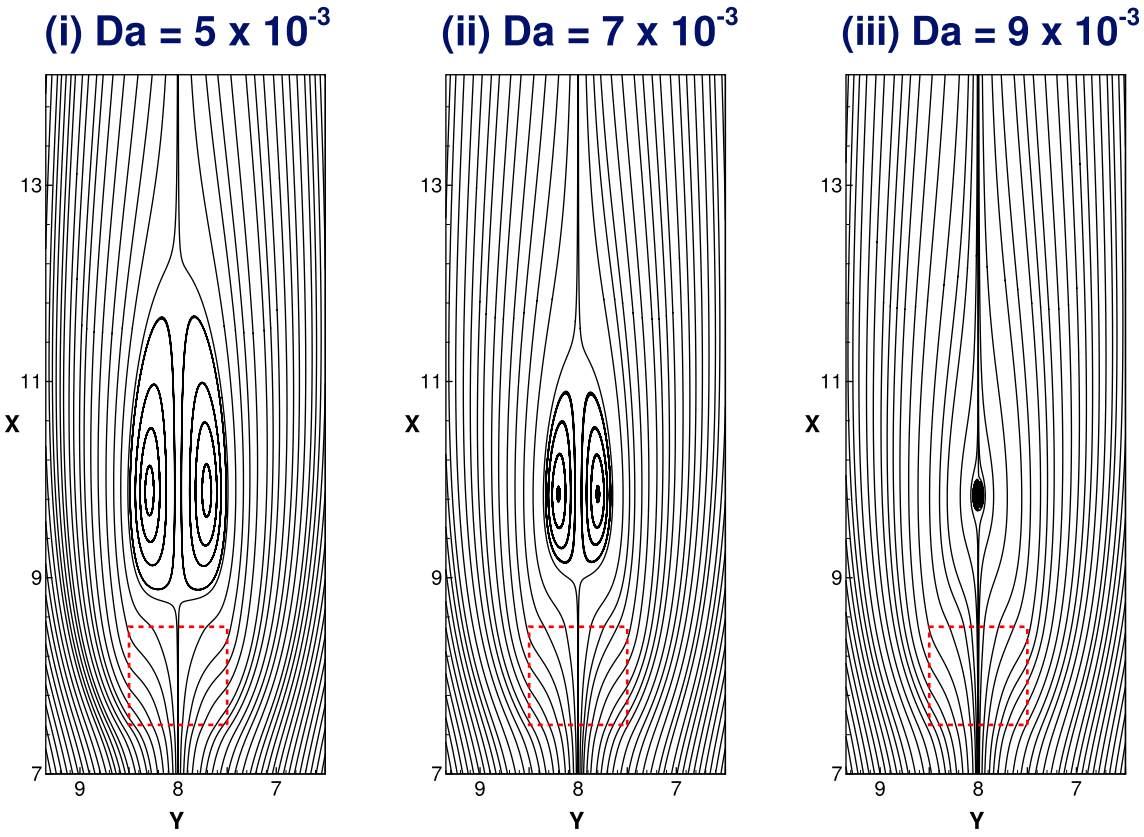

Fig. 9. Progression of the detached wake away from the porous cylinder in the Da_H zone at $Re = 50$.

the fore-body and aft-body shapes seem to govern the occurrence of jump in flow parameters. Square and circular cross-sections lie closer to bluffness, while triangular, trapezoidal and diamond cross-sections appear to be streamlined bodies. Hence, from the current results, published results (Vijaybabu et al., 2018; Vijaybabu et al., 2018b) and literature, it can be discerned that surface area of front and rear faces of the porous cylinder governs the pressure gradient across the body, rather the pressure drag force. The anomalous trend displayed in flow parameters for porous bluff bodies, therefore, has a close relation with its shape. If the porous body cross-section lies closer to bluffness, then the possibilities of jump in flow parameters seem to be larger than that for more streamlined shapes.

5.4. Root mean square lift coefficient ($(C_L)_{rms}$)

After the above detailed qualitative visualisation on flow characteristics in the transition from steady to unsteady flow regime given in Sec. 5.2, a quantitative discussion would cement the understanding of onset of vortex shedding in flow across the porous square cylinder. A quantitative representation of the variation of vortex shedding intensity is represented in terms of $(C_L)_{rms}$ at various Reynolds number and Darcy number values in Fig. 11. At $Re = 41$, due to less momentum, the flow remains steady for all the permeability zones. Unsteadiness is evident in a part of Da_M zone for $Re = 42$ and 43, while the flow remains steady elsewhere. Vortex shedding is evident for $Re = 44$ in Da_L and Da_M zones, which is suppressed early at $Da = 3 \times 10^{-3}$ and remains steady thereafter in the Da_H zone. As the velocity is increased further i.e., at higher Re, this mitigation delays to $Da = 5 \times 10^{-3}$, while shedding of vortices is lucid in the entire Da_L and Da_M zones and no vortices are to be seen in Da_H zone. Interestingly, due to rising Darcy number, $(C_L)_{rms}$ increases instead of decreasing with increase in permeability, contradictory to the logic offered by permeable bodies. However, the rise in $(C_L)_{rms}$ is seen to stall at 10^{-3} in Da_M zone and the role of porous media over flow control strengthens thereafter in Da_H zone.

5.5. Drag ratio (C_{DR})

It is well-known that the drag force on a body decreases as the momentum is increased, due to thinner viscous boundary layer. Accordingly, for a particular Da, the dimensionless drag coefficient exhibits a linear trend as Re is incremented. In order to provide a better insight on the role of permeability levels on drag force acting on the porous cylinder, drag ratio variation is described through Fig. 12. Drag ratio is calculated by normalising mean value of the drag coefficient of a porous cylinder with that of its solid counterpart (in this case $Da = 10^{-6}$), for a particular Re. For the Da_L zone, with increasing Re, the tendency of impermeability increases. Apparently, the slope of the C_{DR} curve steepens with increasing velocity in this zone. This trend is further met a steep jump in the Da_M zone, where a sudden rise in the drag ratio is witnessed. This jump is in line with that reported in the lift coefficient evolution and $(C_L)_{rms}$. The jump succumbs between 3×10^{-3} and 5×10^{-3} and a downfall in the drag ratio is seen due to the porous media authority over flow in Da_H zone. Since, the form drag is found to be less in this flow regime, the overall result is that the jump in drag ratio occurs more steeply at $Da = 10^{-4}$ and further the jump stalls faster at $Da \geq 10^{-3}$. The gradient of downfall increases with Re due to increasing velocity, facilitating reduction in viscous resistance to the flow in porous zone.

5.6. Recirculation length (L_R)

Recirculation length represents the length of standing wakes behind the porous cylinder, measured from trailing edge of the cylinder. In the case of unsteady simulations, time-averaging is performed over one cycle of oscillation of lift coefficient to obtain representative qualitative and quantitative data for comparison with steady-state simulations. Accord-

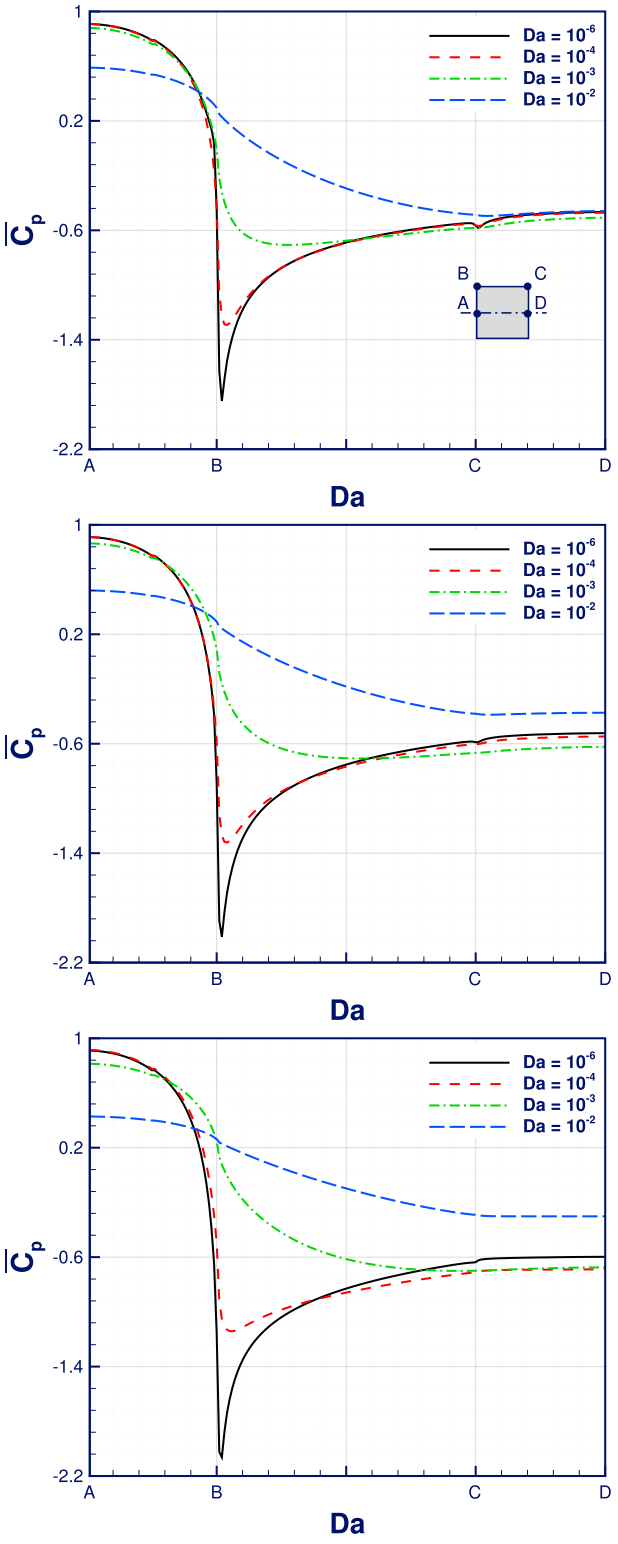

Fig. 10. Time-averaged coefficient of pressure ($\overline{C_p}$) distribution on the porous cylinder surface at different permeability levels, *Da* and Reynolds number, *Re* = (a) 50, (b) 90 and (c) 150.

ingly, the variation of L_R is plotted in Fig. 13 for different values of *Re* and *Da*. A general convention dictates that, in steady flow regime, wake length increases with *Re*. However, the unsteady time-averaged wake length decreases with *Re* and the wake width increases (Yoon et al., 2010), which graphically dictates the intensity of vortex shedding over time, as seen in Sec. 5.2. In the Da_L zone, L_R increases with *Re* up to

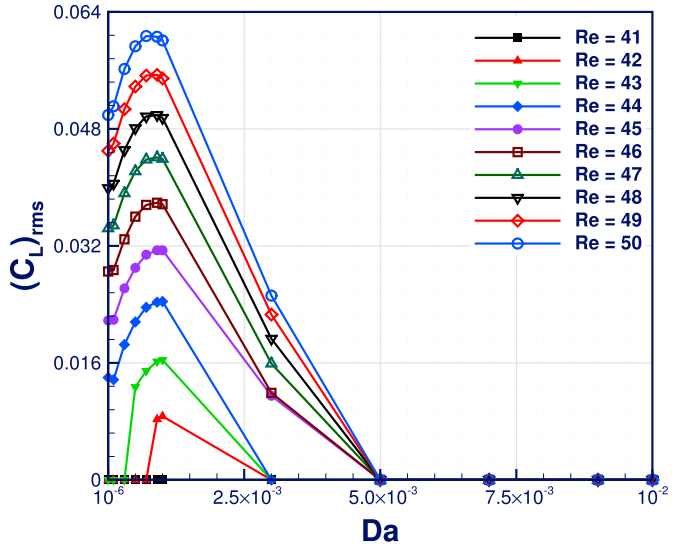

Fig. 11. Variation of root mean square of coefficient, $(C_L)_{rms}$ at different values of Darcy number, *Da* and Reynolds number, *Re*.

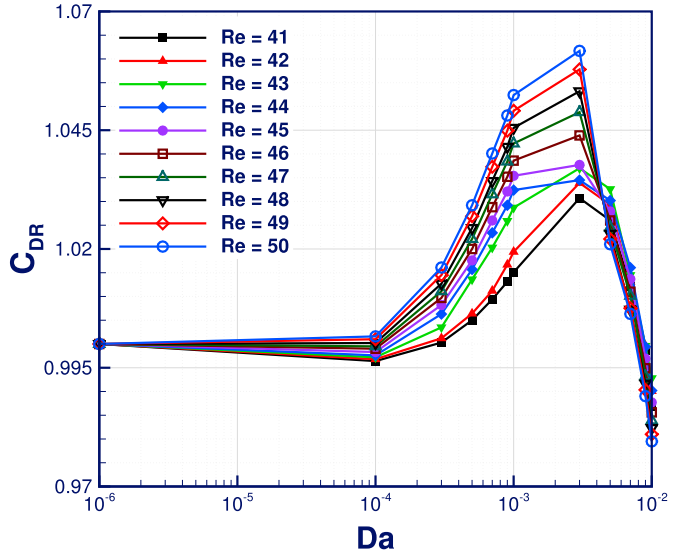

Fig. 12. Drag ratio (C_{DR}) values at different permeability levels, *Da* and Reynolds number, *Re* for the flow around and through a permeable square cylinder.

$Re = 43$ and reduces beyond, indicating the onset of vortex shedding. In the Da_M zone, a mixed trend is seen, wherein the onset of vortex shedding seems to occur early as the permeability level is enhanced. A maximum L_R is reported for $Da = 10^{-3}$ at $Re = 42$ and furthermore, shedding of vortices occur. At even higher permeability levels, a delay in vortex shedding initiation is clear, while at $Da = 3 \times 10^{-3}$ it occurs at $Re = 45$. In the Da_H zone, as seen above, no vortex shedding appears and hence, at a permeability level there exists a direct proportion between L_R and *Re*. At higher permeability levels, as entrainment of fluid through the cylinder increases, the standing wakes move downstream i.e. away from the cylinder. The length and width, of this detached wake decreases seriously with increased momentum and it vanishes completely in between $9 \times 10^{-3} \leq Da \leq 10^{-2}$.

5.7. Strouhal number (St)

The frequency of vortex shedding is clearly indicated by a non-dimensional entity called Strouhal number. In continuation to the

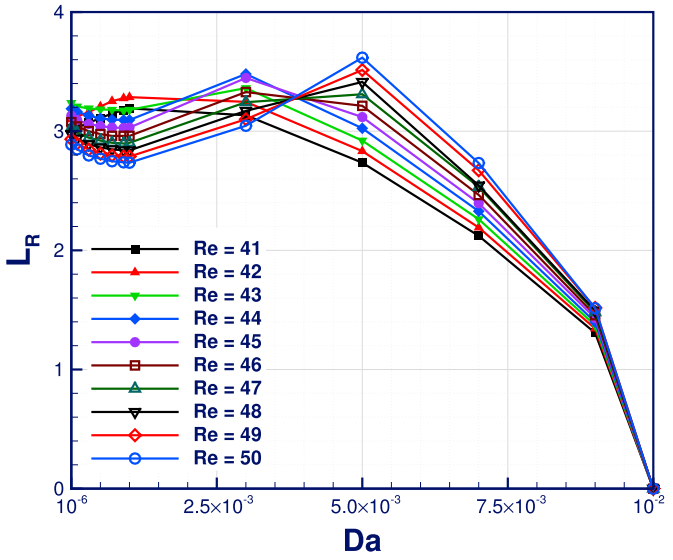

Fig. 13. Wake length, L_R at various Reynolds number, *Re* for different levels of permeability for the flow across a porous square cylinder.

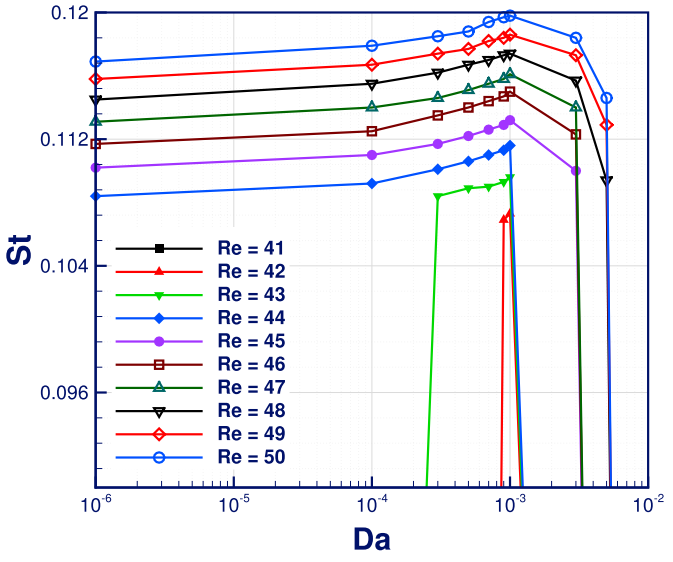

Fig. 14. Strouhal number, *St* as a function of Darcy number, *Da* and Reynolds number, *Re* for the flow across a porous square cylinder.

above discussion, on the onset of vortex shedding, *St* variation at different *Re* and *Da* values gives more comprehensive details on the critical *Re* value for different permeability levels. In general, as more fluid is pumped across the cylinder, frequency of vortex shedding intensifies as the Reynolds number is increased for a given permeability level. The variation of *St* with Darcy number is given in Fig. 14. The flow remains steady at all *Da* values for $Re = 41$ and no trace of unsteadiness is seen. However, in the Da_M zone, near the jump region a minute vortex shedding frequency is reported. But this immediately gets suppressed beyond $Da = 10^{-3}$, as more fluid enters the cylinder for the same values of *Re*, dissipating the unsteadiness of the flow. A sudden jump in the Strouhal number value at $Re = 43$ is witnessed in the same permeability zone, wherein vortex shedding occurs for a lower value of permeability. As *Re* is further increased, the flow becomes unsteady at lower permeability values, the frequency of oscillation augments even after increasing *Da*. Clearly the 'jump' in flow characteristics in the Da_M zone is affecting the porous media's control over flow negatively. As the permeability level approaches Da_H zone, with fluid flowing through the cylinder

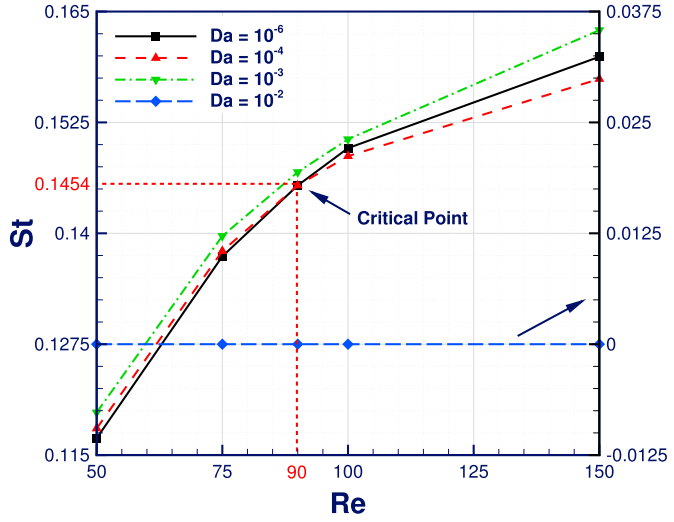

Fig. 15. Strouhal number, *St* as a function of Reynolds number, *Re* at various Darcy numbers, $Da = 10^{-6} - 10^{-2}$. Line representing $Da = 10^{-2}$ data trends uses the scale at right as shown by arrow.

abundantly, reduction in Strouhal number value is apparent. Higher permeability levels of $Da = 3 \times 10^{-3}$, 4×10^{-3} and 5×10^{-3} are required to stabilise the flow at $Re = 43 - 44$, $45 - 47$ and $48 - 50$, respectively.

Evidently, with rising permeability level, *St* increases instead of decreasing for a particular Reynolds number, the trend succumbs only beyond $Da = 10^{-3}$. With a curiosity to further investigate this anomalous behaviour, simulations were run in the unsteady flow regime at $Re = 50, 75, 90, 100$ and 150 and the trend is displayed in Fig. 15. The difference in frequency of vortex shedding at $Da = 10^{-4}$ and $Da = 10^{-6}$ tends to reduce with increasing momentum, and it almost nullifies at $Re = 90$. Furthermore, this difference in *St* diverges with enhanced momentum transfer, which hints that the authority of porous media over flow is partially regained. It is considered 'partial' only because the drag coefficient at this permeability level remains higher than the lower Darcy number flow, as discussed in Sec. 5.3. Meanwhile, *St* at $Da = 10^{-3}$ stays higher that the lower permeability levels and the difference also diverges with higher *Re*. But in the Da_H zone, abrupt suppression of flow unsteadiness is lucid, and the flow remains steady even at $Re = 150$.

For the range of flow parameters considered in the present study, following correlation has been developed by performing a non-linear regression the entire data set:

$$St = 0.317 \cdot \left(ln(Re)^{0.140}\right) \cdot \left(ln(Da)^{-0.004}\right) - 0.055. \quad (9)$$

The above correlation provides a satisfactory regression coefficient value of 0.971, wherein the average and maximum deviation between the actual data and correlation results are 1.004% and 2.572%, respectively.

6. Conclusions

Onset of vortex shedding in the flow across a two-dimensional porous square cylinder, placed in a uniform flow, has been numerically analysed in this study. The generic pimpleFoam solver of OpenFOAM has been modified with the extended Darcy-Brinkman-Forchheimer model and the inclusion of porosity term in the momentum equation to account for the superficial speed of flow in the porous region. In précis, a coherent loss of porous media's control over suppression of flow unsteadiness for the square bluff shape is evident. In the flow transition regime for a porous square cylinder i.e. $Re = 41 - 50$, in the Da_L zone, the body mimics its solid counterpart by allowing very less or no fluid through it. Hence, the critical Reynolds number for the initiation of flow unsteadiness remains

very close to that of a solid square cylinder. In the Da_M zone, where steadiness in flow could be expected due to dampening effect of porous bodies, a jump in flow parameters is seen, which pre-pones vortex shedding initiation. The unsteady flow regime was further looked into, and it was seen that only after $Re = 90$, a decrease in intensity and frequency of shedding of vortices is seen for $Da = 10^{-4}$. But the jump still exists when the Darcy number is raised up to $Da = 10^{-3}$. The porous cylinder seems to delay the onset of and suppress vortex shedding only in the Da_H zone ($Da > 5 \times 10^{-3}$). On the basis of present results, published results (Vijaybabu et al., 2018; Vijaybabu et al., 2018b) and literature, it is discerned that surface area of front and rear faces of the porous cylinder governs the pressure gradient across the body, rather the pressure drag force. The anomalous trend exhibited in flow parameters for porous square cylinder, therefore, has a close relation with its shape. In general, if the porous body cross-section lies closer to bluffness, then the possibilities of jump in flow parameters seem to be larger than that for more streamlined shapes. Critical values of Reynolds number at all values of permeability levels considered in the study are given and they match closely with that in the literature for a solid cylinder. If a research scientist or an engineer, interested in applying the porous media theory for computational simplicity of a problem in hand, wish to setup their model as a porous square cylinder, it is highly recommended that they stay in Da_M zone if flow incentives can be compromised and heat transfer augmentation is the main purpose. Otherwise, Da_H zone i.e., higher values of permeability can provide both, flow control and improved heat dissipation rate (due to higher surface area).

Acknowledgement

One of the authors, S. Dhinakaran, gratefully acknowledges the financial aid received from Council of Scientific & Industrial Research (CSIR), Government of India through a project Grant (Project Reference No. 22(0642)/13/EMR-II) for carrying out this work. The authors are highly obliged to the reviewers for their insightful comments and suggestions.

References

Belloli, M., Rosa, L., Zasso, A., 2014. Wind loads and vortex shedding analysis on the effects of the porosity on a high slender tower. J. Wind Eng. Ind. Aerod. 126, 75–86.
Bhattacharyya, S., Singh, A., 2011. Reduction in drag and vortex shedding frequency through porous sheath around a circular cylinder. Int. J. Numer. Meth. Fluid. 65 (6), 683–698.
Bhattacharyya, S., Dhinakaran, S., Khalili, A., 2006. Fluid motion around and through a porous cylinder. Chem. Eng. Sci. 61 (13), 4451–4461.
Bruneau, C.-H., Mortazavi, I., 2008. Numerical modelling and passive flow control using porous media. Comput. Fluids 37 (5), 488–498.
Chen, X., Yu, P., Winoto, S., Low, H.-T., 2008. Numerical analysis for the flow past a porous square cylinder based on the stress-jump interfacial-conditions. Int. J. Numer. Meth. Heat Fluid Flow 18 (5), 635–655.
Chen, X., Yu, P., Winoto, S., Low, H., 2009. Numerical analysis for the flow past a porous trapezoidal-cylinder based on the stress-jump interfacial-conditions. Int. J. Numer. Meth. Heat Fluid Flow 19 (2), 223–241.
Cheung, J., Melbourne, W., 1988. Wind loading on a porous roof. J. Wind Eng. Ind. Aerod. 29 (1–3), 19–28.
Dhinakaran, S., Ponmozhi, J., 2011. Heat transfer from a permeable square cylinder to a flowing fluid. Energy Convers. Manag. 52 (5), 2170–2182.
Franke, R., Rodi, W., Schönung, B., 1990. Numerical calculation of laminar vortex-shedding flow past cylinders. J. Wind Eng. Ind. Aerod. 35, 237–257.
Hasan, A., Foss, B., Sagatun, S., 2012. Flow control of fluids through porous media. Appl. Math. Comput. 219 (7), 3323–3335.
Henderson, R.D., 1995. Details of the drag curve near the onset of vortex shedding. Phys. Fluids 7 (9), 2102–2104.
Holdich, R., 2002. Fundamentals of Particle Technology. Midland Information Technology and Publishing. ISBN 0954388100.
Jackson, C., 1987. A finite-element study of the onset of vortex shedding in flow past variously shaped bodies. J. Fluid Mech. 182, 23–45.
Jue, T.C., 2004. Numerical analysis of vortex shedding behind a porous square cylinder. Int. J. Numer. Meth. Heat Fluid Flow 14 (5), 649–663.
Khalili, A., Liu, B., Javadi, K., Morad, M.R., Kindler, K., Matyka, M., Stocker, R., Koza, Z., 2010. Application of porous media theories in marine biological modeling. In: Porous Media: Applications in Biological Systems and Biotechnology. CRC Press, pp. 365–398.
Kumar, A., Dhiman, A., Baranyi, L., 2016. Fluid flow and heat transfer around a confined semi-circular cylinder: onset of vortex shedding and effects of Reynolds and Prandtl numbers. Int. J. Heat Mass Tran. 102, 417–425.
Lankadasu, A., Vengadesan, S., 2008. Onset of vortex shedding in planar shear flow past a square cylinder. Int. J. Heat Fluid Flow 29 (4), 1054–1059.
Lee, S.-J., Kim, H.-B., 1998. Velocity field measurements of flow around a triangular prism behind a porous fence. J. Wind Eng. Ind. Aerod. 77, 521–530.
Liu, H., Azarpeyvand, M., 2016. Passive control of tandem cylinders flow and noise using porous coating. In: 22nd AIAA/CEAS Aeroacoustics Conference, p. 2905.
Mimeau, C., Mortazavi, I., Cottet, G.-H., 2017. Passive control of the flow around a hemisphere using porous media. Eur. J. Mech. B Fluid 65, 213–226.
Noymer, P.D., Glicksman, L.R., Devendran, A., 1998. Drag on a permeable cylinder in steady flow at moderate Reynolds numbers. Chem. Eng. Sci. 53 (16), 2859–2869.
Paul, I., Prakash, K.A., Vengadesan, S., 2014. Onset of laminar separation and vortex shedding in flow past unconfined elliptic cylinders. Phys. Fluids 26 (2), 023601.
Rashidi, S., Bovand, M., Pop, I., Valipour, M., 2014. Numerical simulation of forced convective heat transfer past a square diamond-shaped porous cylinder. Transport Porous Media 102 (2), 207–225.
Schumm, M., Berger, E., Monkewitz, P.A., 1994. Self-excited oscillations in the wake of two-dimensional bluff bodies and their control. J. Fluid Mech. 271, 17–53.
Senthil Kumar, N., Biswas, G., 2008. A finite element study of the onset of vortex shedding in a flow past two-dimensional circular cylinder. Prog. Comput. Fluid Dynam. Int. J. 8 (5), 288–298.
Sharma, A., Eswaran, V., 2004. Heat and fluid flow across a square cylinder in the two-dimensional laminar flow regime. Numer. Heat Tran., Part A: Applications 45 (3), 247–269.
Sohankar, A., Norberg, C., Davidson, L., 1995. Numerical simulation of unsteady flows around a square two-dimensional cylinder. In: Twelfth Australian Fluid Mechanics Conference, pp. 517–520.
Sohankar, A., Norbergb, C., Davidson, L., 1997. Numerical simulation of unsteady low-Reynolds number flow around rectangular cylinders at incidence. J. Wind Eng. Ind. Aerod. 69, 189–201.
Sohankar, A., Norberg, C., Davidson, L., 1998. Low-Reynolds-number flow around a square cylinder at incidence: study of blockage, onset of vortex shedding and outlet boundary condition. Int. J. Numer. Meth. Fluid. 26 (1), 39–56.
Sohankar, A., Norberg, C., Davidson, L., 1999. Simulation of three-dimensional flow around a square cylinder at moderate Reynolds numbers. Phys. Fluids 11 (2), 288–306.
Swaminathan, V.V., Gannavaram, S., Li, S., Hu, H., Yeom, J., Wang, Y., Zhu, L., 2013. Microfluidic platform with hierarchical micro/nanostructures and SELEX nucleic acid aptamer coating for isolation of circulating tumor cells. In: Nanotechnology (IEEE-NANO). IEEE, pp. 370–373, 2013 13th IEEE Conference on.
Vijaybabu, T.R., Anirudh, K., Dhinakaran, S., 2017. Mixed convective heat transfer from a permeable square cylinder: a lattice Boltzmann analysis. Int. J. Heat Mass Tran. 115, 854–870.
Vijaybabu, T.R., Anirudh, K., Dhinakaran, S., 2018. LBM simulation of unsteady flow and heat transfer from a diamond-shaped porous cylinder. Int. J. Heat Mass Tran. 120, 267–283.
Vijaybabu, T.R., Anirudh, K., Dhinakaran, S., 2018b. Lattice Boltzmann simulations of flow and heat transfer from a permeable triangular cylinder under the influence of aiding buoyancy. Int. J. Heat Mass Tran. 117, 799–817.
Weller, H.G., Tabor, G., Jasak, H., Fureby, C., 1998. A tensorial approach to computational continuum mechanics using object-oriented techniques. Comput. Phys. 12 (6), 620–631.
Wu, H.-W., Wang, R.-H., 2010. Convective heat transfer over a heated square porous cylinder in a channel. Int. J. Heat Mass Tran. 53 (9), 1927–1937.
Yoon, D.-H., Yang, K.-S., Choi, C.-B., 2010. Flow past a square cylinder with an angle of incidence. Phys. Fluids 22 (4), 043603.
Yu, P., Zeng, Y., Lee, T., Bai, H., Low, H., 2010. Wake structure for flow past and through a porous square cylinder. Int. J. Heat Fluid Flow 31 (2), 141–153.
Zaripov, S., Mukhametzanov, I., Grinshpun, S., 2016. Numerical studies on the performance of an aerosol respirator with faceseal leakage. In: IOP Conference Series: Materials Science and Engineering, vol 158. IOP Publishing, 012100.